ARTICLES
PUBLISHED ONLINE: 17 JULY 2017 | DOI: 10.1038/NNANO.2017.131
nature nanotechnology

Controlling energy flow in multimetallic nanostructures for plasmonic catalysis

Umar Aslam, Steven Chavez and Suljo Linic*

It has been shown that photoexcitation of plasmonic metal nanoparticles (Ag, Au and Cu) can induce direct photochemical reactions. However, the widespread application of this technology in catalysis has been limited by the relatively poor chemical reactivity of noble metal surfaces. Despite efforts to combine plasmonic and catalytic metals, the physical mechanisms that govern energy transfer from plasmonic metals to catalytic metals remain unclear. Here we show that hybrid core–shell nanostructures in which a core plasmonic metal harvests visible-light photons can selectively channel that energy into catalytically active centres on the nanostructure shell. To accomplish this, we developed a synthetic protocol to deposit a few monolayers of Pt onto Ag nanocubes. This model system allows us to conclusively separate the optical and catalytic functions of the hybrid nanomaterial and determine that the flow of energy is strongly biased towards the excitation of energetic charge carriers in the Pt shell. We demonstrate the utility of these nanostructures for photocatalytic chemical reactions in the preferential oxidation of CO in excess H_2. Our data demonstrate that the reaction occurs exclusively on the Pt surface.

It has been demonstrated recently that plasmonic metal nanoparticles illuminated with relative low-intensity light can perform photochemical transformations[1–5]. These discoveries have led to a new field of chemical conversion termed plasmonic catalysis. Plasmon-driven chemical conversion has been demonstrated mainly on noble metal nanoparticles (Au, Ag and Cu) for some chemical transformations[6–8]. These nanomaterials exhibit a strong localized surface plasmon resonance (LSPR) that is characterized by a high extinction of light and large electric fields at the surface[9–11]. The combination of these two effects leads to high rates of formation of energetic charge carriers in the nanoparticles, which can result in chemical transformations[12–14].

The central obstacle to expanding the use of plasmonic catalysis is that it has been limited to chemical transformations that can be performed only on the surfaces of the noble metals, which are inherently not very chemically reactive[15,16]. We and others have been attempting to understand the nanoscopic mechanisms of plasmon decay in metallic nanoparticles, with the ultimate objective to control this decay process[17–21]. In particular, we were interested in designing functioning nanostructures in which a plasmonic material concentrates the light energy and this energy is efficiently directed towards a more-active catalytic material. We conceptualized recently the design of such a hybrid plasmonic metal nanostructure[12]. We postulated that a hybrid nanostructure that would meet the critical requirements of such a system should contain a core plasmonic nanoparticle (a metal with a low imaginary dielectric function at the LSPR (visible light) frequencies) surrounded by a very thin shell of a more chemically active material (catalytic surface sites), characterized by a significantly larger imaginary dielectric function at the LSPR frequency. A material with these dielectric properties has two desired physical features: (1) because of the presence of a large plasmonic core, it can concentrate electromagnetic energy in the LSPR modes and (2) the energy stored in the LSPR modes can be dissipated selectively by forming energetic charge carriers (energetic electron–hole (e–h) pairs) in the thin shell of the metal with the large imaginary dielectric function. The larger imaginary dielectric function implies that the rate of energy dissipation (that is, the decay of the LSPR modes) through the formation of energetic charge carriers is larger compared with the material with a lower imaginary dielectric function[22]. We hypothesized that this hybrid nanostructure design would allow for a strong concentration of the electromagnetic energy and its preferential dissipation through the surface atoms that perform the chemical transformation. In addition to these dielectric considerations, to preserve the core–shell architecture in the reactive environments for practical catalytic applications, the core and shell metals should not be miscible.

In this contribution, we describe a systematic design of such a hybrid nanostructure in the form of core–shell nanoparticles that contain a very thin shell (~1 nm) of epitaxially grown Pt on the surface of cubic Ag nanoparticles. We performed experimental and theoretical studies that showed unambiguously that the optical energy collected under the LSPR conditions by these nanostructures is preferentially dissipated through the Pt shell where the chemical reaction takes place. We demonstrate the utility of these hybrid nanostructures in the preferential oxidation of CO in the presence of abundant H_2, a chemical process that is relevant for the technology of hydrogen fuel cells[23,24]. These studies provide us with (1) a clear pathway to marry plasmonic and catalytic functions in one material, which allows us to expand the utilization of plasmonic catalysis to materials other than noble metals, (2) a new strategy to synthesize such core–shell metallic nanostructures and (3) physical insights into the flow of energy in multicomponent plasmonic systems.

A few reports of hybrid systems have contested the joint action of plasmonic nanoparticles and catalytically active metal clusters[25–29]. These systems mainly employed plasmonic nanoparticles (either free[25,26] or surrounded by thin oxide shells[27,28]) randomly decorated with smaller catalytically active metal nanoclusters. In these hybrid systems, it is difficult to separate completely the optical and catalytic function of the two different components. This makes it very challenging to demonstrate conclusively that the plasmonic chemistry does not take place on the plasmonic particle, or at the interfacial sites between the plasmonic metal and the clusters, or that it results

Department of Chemical Engineering, University of Michigan, Ann Arbor, Michigan 48109, USA. *e-mail: linic@umich.edu

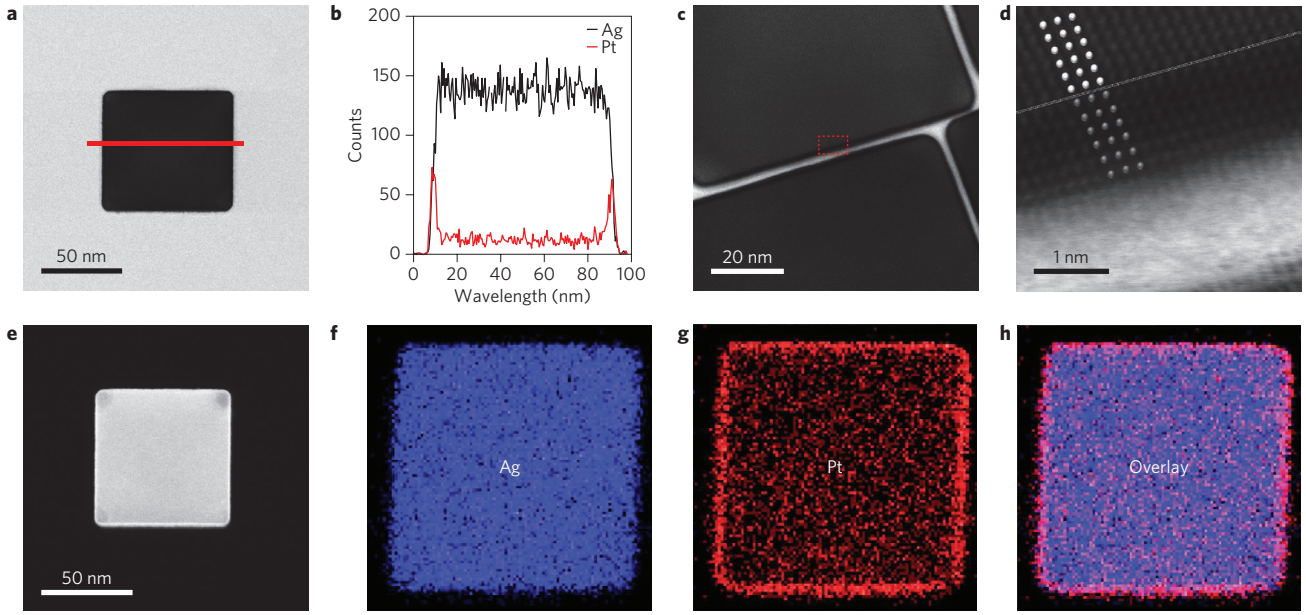

Figure 1 | Characterization of Ag–Pt nanocubes. a, Bright-field TEM image of a single Ag nanocube coated with a thin layer of Pt. **b**, EDS elemental line scan taken along the red line in **a** to demonstrate the elemental composition of the core and shell of the nanocube. **c**,**d**, High-resolution and atomic-resolution bright-field TEM images. The thin Pt shell appears darker in contrast owing to the higher elemental weight of Pt. The Ag and Pt atoms are highlighted in **d**, which clearly shows the boundary between the two materials. **e**–**h**, Dark-field STEM image of a representative core–shell nanocube (**e**) and EDS elemental maps of Ag (**f**), Pt (**g**) and an overlay of the two (**h**) demonstrate the complete coverage of Ag by Pt.

from light-induced changes in the oxidation state of the plasmonic metal or the oxide shell[8,30,31]. In addition, these designs of the hybrid materials make it difficult to quantify the flow of energy to the active site from the plasmonic nanoparticle. We believe the model system used herein, in which plasmonic nanoparticles are completely covered by very thin shells of a catalytically active metal, is the ideal platform for performing these experiments as it allows for complete decoupling of the optical and catalytic functions.

Nanoparticle synthesis and characterization

We synthesized hybrid nanostructures by developing a synthetic approach that allows us to surround Ag nanocube cores (~75 nm in length) completely with thin Pt shells (~1 nm thickness). To synthesize these core–shell nanostructures we developed a seed-mediated colloidal synthesis approach in which Ag nanocube seeds were coated with Pt by reducing a Pt-metal complex precursor onto the seeds (Supplementary Section 1 gives the complete synthesis details, which include an approach to vary the shell thickness).

The geometry characterization studies in Fig. 1 unambiguously show that the synthesis approach yields Ag nanocubes covered by a thin Pt shell. A bright-field transmission electron micrograph (TEM) of a representative Ag–Pt core–shell nanocube is shown in Fig. 1a. The high-resolution TEM image in Fig. 1c (atomic resolution indicated in Fig. 1d (outline in Fig. 1c)) shows that the Pt shell thickness in these nanoparticles was approximately six atomic layers of Pt, which corresponds to 1.2 ± 0.2 nm. A dark-field scanning transmission electron microscope (STEM) image of a core–shell nanoparticle is shown in Fig. 1e. An energy-dispersive X-ray spectroscopy (EDS) elemental line scan across a single representative nanoparticle (Fig. 1b) and the EDS elemental mapping of Ag and Pt in Fig. 1f–h show that Pt atoms cover the Ag nanocube (75 nm edge length). Additional characterization that demonstrates the high yield of the core–shell structures and the ability to tune shell thickness are provided in Supplementary Figs 2–4. To establish that the surface Pt atoms of the Ag–Pt core–shell nanocubes are chemically identical to the surface Pt atoms of monometallic Pt nanoparticles, we characterized the CO adsorption (as a probe molecule) on the Ag–Pt nanocubes and on Pt nanoparticles (~5 nm in diameter) using diffuse-reflectance infrared Fourier transform spectroscopy (DRIFTS). These data (Supplementary Fig. 5) show that the vibrational frequency of CO adsorbed on the Ag–Pt core–shell nanocubes and on monometallic Pt are centred at 2,056 cm^{-1} and at 2,060 cm^{-1}, respectively, which indicates that the two Pt surfaces are chemically similar. The small difference in the CO vibrational frequency is caused by the lower coordination of Pt(100) sites on the Ag–Pt nanocubes compared with that of Pt(111) sites on the Pt nanoparticles.

Characterizing plasmon excitation and decay pathways

We analysed the optical properties of these hybrid nanostructures by measuring their extinction, absorption and scattering characteristics and comparing these with the optical behaviour of Ag nanocubes of identical size and shape (Supplementary Section 2 gives the experimental details). The data in Fig. 2a show that the introduction of the thin Pt shell on the Ag core only slightly affects the optical extinction of the nanostructure. The extinction peak caused by the excitation of LSPR is clearly preserved. Small shifts in the position and width of the LSPR peak compared with those of pure Ag nanocubes result from the Pt-induced changes in the dielectric environment because of the presence of the Pt shell. To determine whether the thin Pt shells themselves contribute to the optical extinction, acid leeching was used to remove Ag from the cores of the Ag–Pt nanoparticles in a representative sample, to leave behind thin-shelled Pt cages (Supplementary Fig. 7). Optical characterization of these cages showed that the Pt shell does not display any optical extinction in the visible range (Supplementary Fig. 8). Furthermore, we used an integrating optical sphere to measure the absorption and scattering of the pure Ag nanocubes and the Ag–Pt core–shell nanocubes. The data in Fig. 2b,c show that the introduction of even a very thin Pt shell fundamentally changes the dominant channel for plasmon decay. The data in Fig. 2b show that photon scattering is the dominant pathway for plasmon decay in pure Ag nanocubes, which is consistent with

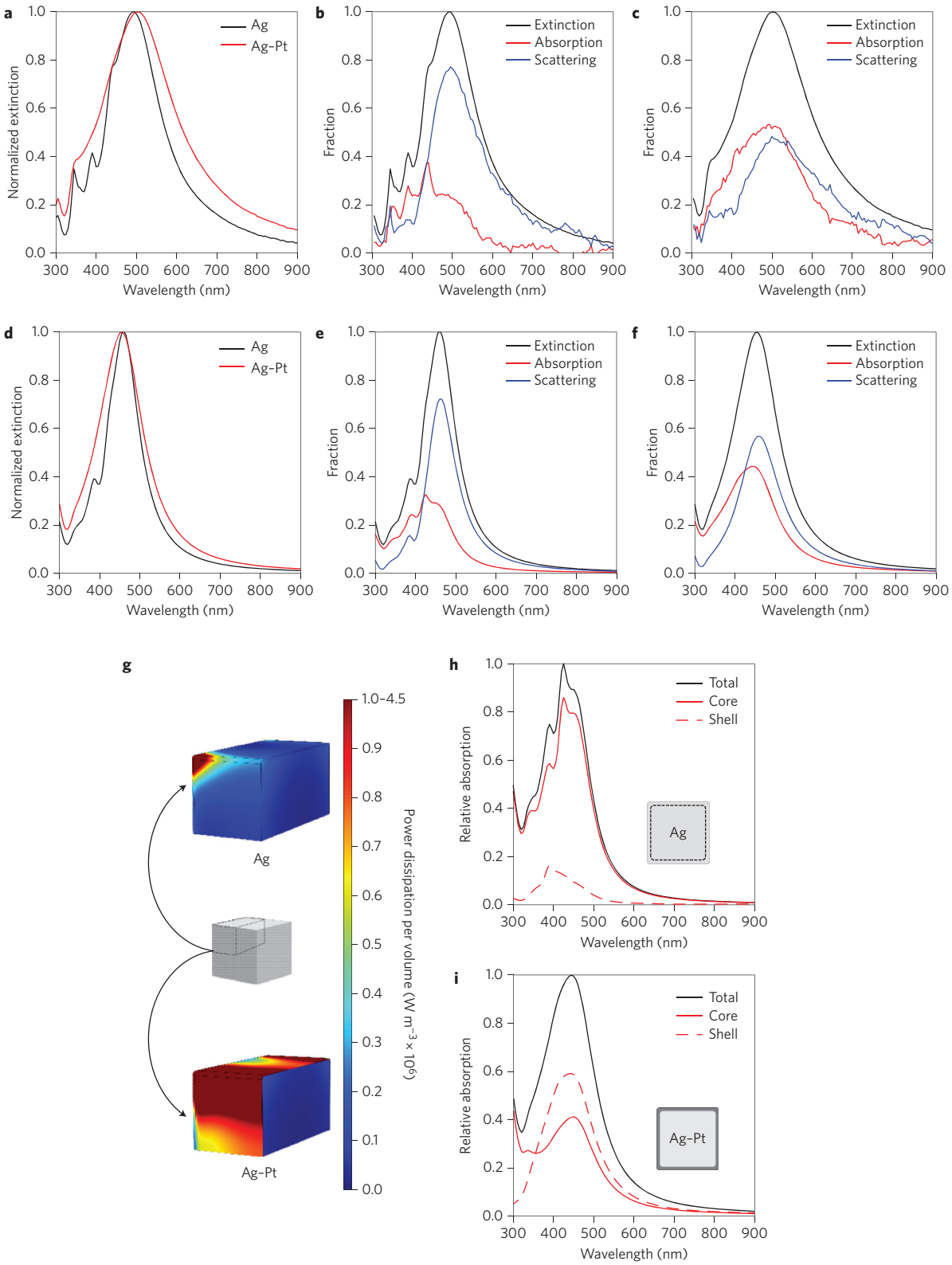

Figure 2 | Measured and calculated optical extinction, absorption, and scattering of Ag and Ag–Pt nanocubes. a, Measured extinction of the Ag nanocubes and Ag–Pt core–shell nanocubes. **b**, Measured fractional Ag nanocube absorption and scattering. **c**, Measured fractional Ag–Pt nanocube absorption and scattering. **d**, Calculated extinction of Ag nanocubes (76.2 nm edge length) and Ag–Pt core–shell nanocubes (75 nm edge length Ag core plus 1.2 nm Pt shell). **e**, Calculated fractions of Ag nanocube absorption and scattering. **f**, Calculated fractions of the Ag–Pt nanocube absorption and scattering. **g**, Heat maps of the power dissipation per volume at the LSPR peak (455 nm) for the Ag nanocube and at the LSPR peak (460 nm) for the Ag–Pt nanocube. The source field was 1 V m^{-1} at the resonant frequency, which for a free space amounts to 2.6×10^{-4} mW cm^{-2}. **h**, Fraction of the power absorbed in the 75 nm thick 'core' and the 1.2 nm thick 'shell' of a pure Ag nanocube. The inset depicts the size of the Ag 'core' and Ag 'shell'. **i**, Fraction of the power absorbed in the 75 nm thick Ag 'core' and the 1.2 nm thick Pt 'shell' of an Ag–Pt nanocube. The inset depicts the size of the Ag 'core' and Pt 'shell'.

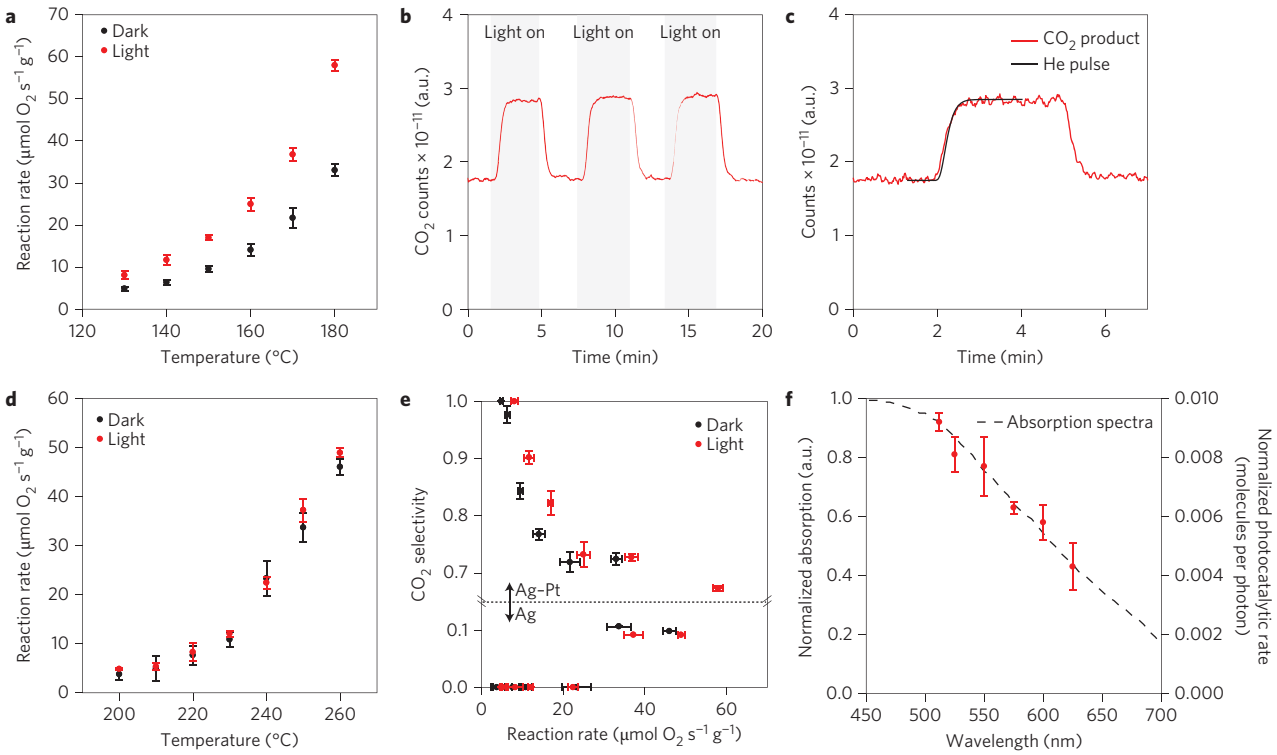

Figure 3 | Photocatalytic reactor studies. a, Reaction rate versus temperature for preferential CO oxidation in excess H_2 on Ag–Pt core–shell nanocubes under light-off and light-on conditions. **b**, Fast-response mass spectrometry analysis of CO_2 produced during the cycling of light-on and light-off conditions. **c**, Pulse experiments characterize the time response of the Ag–Pt catalyst to illumination compared with the time response of the system to an inert He pulse introduced at the inlet of the reactor. **d**, Reaction rate versus temperature for preferential CO oxidation in excess H_2 on an Ag nanocube catalyst. **e**, Selectivity towards CO oxidation versus reaction rate on Ag–Pt core–shell nanocubes and Ag nanocubes (note the break in the vertical axis). No CO_2 was detectable at the low reaction rates on Ag, that is, this catalyst preferentially oxidizes H_2 rather than CO. **f**, Normalized absorption spectra of the Ag–Pt nanocube catalyst, obtained under reaction conditions, plotted as a function of the wavelength-dependent photocatalytic reaction rate. The photocatalytic reaction rate was normalized by dividing by the photon flux at each wavelength. Error bars in each plot represent one s.d. from the average value.

previous measurements for Ag nanoparticles of this size[32,33]. The data in Fig. 2c show that by introducing a thin Pt shell in our design, photon absorption (the formation of energetic e–h pairs) becomes a critical plasmon-decay pathway. Based on these experimental data, we hypothesized that the introduction of Pt introduces a faster plasmon decay channel through the Pt shell and that a large fraction of the electromagnetic energy concentrated in the nanostructure is dissipated through the thin Pt shell via the formation of energetic charge carriers (e–h pairs).

To shed light on the optical behaviour of these systems, we performed electrodynamic finite element method (FEM) simulations. The model system used in our FEM simulations is identical to the nanoparticle geometry measured in the TEM studies (Supplementary Section 3 gives the simulation details and absolute extinction, scattering and absorption values). The calculated extinction, absorption and scattering characteristics of pure Ag and the Ag–Pt core–shell nanocubes (Fig. 2d–f) are fully consistent with the experimental measurements, which shows that the extinction is largely unchanged with the introduction of a thin Pt shell and that the absorption is more dominant in the nanomaterials that contain Pt compared with pure Ag. We also used these simulations to analyse the power dissipated (that is, the rate of photon absorption through the formation of energetic charge carriers (e–h pairs)) through the thin Pt shell of an Ag–Pt core–shell nanocube and an Ag shell of the equivalent dimensions on a pure Ag nanocube. Comparing the data in Fig. 2g–i, we find that in the Ag–Pt nanoparticles a large fraction of energy is dissipated through absorption in the Pt shell compared with that in pure Ag, in which the energy dissipated through absorption is relatively low at any part of the nanostructure. For example, FEM simulations show that for a Pt shell of 1.2 nm thickness on a core cube of Ag (edge length 75 nm) the rate of absorption per unit volume in the Pt shell is ~22 times larger than the rate of absorption in the core over the visible-light wavelength range (300–900 nm). In comparison, for the same thickness of an Ag shell in an Ag nanoparticle of identical size and shape, the rate of absorption per unit volume in the shell is only about three times larger than the rate of absorption in the core. A similar analysis of our integrating sphere experimental data shows the rate of absorption per unit volume in a thin Pt shell (1.2 nm) was ~18 times larger than the rate of absorption in the Ag core, in relative agreement with the FEM simulations (Supplementary Section 4 gives the calculation details and additional data).

Performing plasmonic catalysis on Ag–Pt nanocubes

The optical simulations and the optical sphere measurements in Fig. 2 suggest that by positioning a thin Pt shell (~1 nm) on a large Ag core (~75 nm), we create nanostructures in which the process of the formation of energetic charge carriers is largely moved to the Pt shell. Another question that we wanted to explore is whether the energy that is selectively dissipated through the Pt shell can be used to perform chemical work (that is, drive a chemical transformation) on Pt. To address this question, we studied the catalytic preferential CO oxidation reaction in the presence of excess H_2. This is an important chemical reaction used to remove CO from H_2 by selectively oxidizing CO into CO_2. It is well established that Pt can execute this reaction with a high CO

oxidation selectivity, whereas Ag shows a very poor reaction selectivity (that is, on Ag, H_2 is oxidized selectively) and is less active than Pt (refs 34–36). We performed photocatalytic reaction experiments in a packed-bed reactor equipped with a glass window for catalyst illumination using a broadband visible-light source at an intensity of ~400 mW cm^{-2}. Preferential CO oxidation in excess H_2 was performed on the Ag–Pt catalyst with 75% H_2, 2% O_2, 3% CO and balance N_2 at temperatures that ranged from 130 to 180 °C at differential reactant conversions. In addition, control experiments were performed on a monometallic Ag catalyst under the same flow conditions at temperatures the ranged from 200 to 260 °C. Higher temperatures are necessary for that Ag catalyst because the Ag surfaces are less active for the reaction. The catalyst preparation procedure, design of reactor studies, light-source spectrum and pre- and post-reaction catalyst characterization are all provided in Supplementary Section 5.

Data in Fig. 3a show that when the Ag–Pt core–shell catalyst system was illuminated with broadband visible light at a 400 mW cm^{-2} intensity, we observed a significant increase in the reaction rate (the rate is reported in terms of the reacted O_2). This light-induced increase in the reaction rate on the core–shell nanoparticles was reversible (Fig. 3b). Additionally, by comparing the temporal response of the system to light to the temporal response of the system to an inert gas tracer, we concluded that, within the limit of our reactor design and product-detection schemes, the response of the catalyst to the light flux was instantaneous (Fig. 3c). Unlike in the case of the Ag–Pt core–shell nanocubes, illuminating the Ag nanoparticle catalyst that contained Ag nanoparticles of identical size and shape as the Ag–Pt core–shell nanoparticles did not result in any measurable change in the reaction rate (Fig. 3d). Data in Fig. 3e show the selectivity to CO oxidation on the Ag–Pt core–shell nanoparticles and pure Ag as a function of the reaction rate. As expected, the CO oxidation selectivity on Ag is very low, whereas the Ag–Pt core–shell nanoparticles show a very high CO oxidation selectivity characteristic of Pt surfaces for this reaction[34]. Data in Fig. 3f show the normalized photocatalytic reaction rate on the Ag–Pt core–shell nanoparticles measured as a function of light wavelength. In these measurements, optical filters were employed to control the wavelength of photons that impinged on the catalyst. The one-to-one mapping between the normalized photocatalytic rate and the nanoparticle optical absorption caused by LSPR indicates that the excitation of LSPR is responsible for the observed increase in the reaction rate. The data in Fig. 3 conclusively demonstrate that LSPR excitation in multicomponent plasmonic nanostructures can drive chemical reactions on non-plasmonic, catalytically active surface sites. In this particular case, Ag nanocubes, surrounded by a few monolayers of catalytically active Pt, collect the energy of incoming visible light through LSPR excitation and dissipate this energy to the chemically attached Pt catalytic sites, which results in enhanced catalytic rates.

Conclusions

Based on our optical (Fig. 2) and catalytic (Fig. 3) data, we can study the flow of energy in these multicomponent systems that leads to plasmon-driven reactions on non-plasmonic active sites. The incoming electromagnetic radiation excites the LSPR of the multicomponent plasmonic nanostructures, which results in a high overall extinction and elevated electric field intensities near the surface of the nanoparticles. The energy of the LSPR is dissipated through the various available dissipation pathways. These dissipation pathways include photon scattering, as well as absorption events (excitation of energetic charge carriers) at various parts of the nanostructure. In metal nanoparticles, these scattering and absorption events have their characteristic rates; the direct vertical electronic excitations (in metals these are the excitations from *d* states below the Fermi level to *s* states above the Fermi level) have the fastest plasmon-decay channel[18,37]. At visible photon energies, Ag does not allow for the direct vertical *d*-to-*s* transitions because the *d* states in Ag are well below the Fermi level and these electrons cannot be excited by visible photons[38]. On the other hand, Pt supports these fast electronic excitations. By positioning a few layers of Pt on an Ag nanoparticle, we effectively direct the LSPR energy towards selective dissipation through these Pt sites. Furthermore, this LSPR-decay channel is also enhanced by the presence of very high LSPR-induced electric-field intensities at the surface layers of these nanostructures. This flow of energy concentrates a large fraction of electromagnetic energy in the surface Pt atoms, and effectively 'energizing' these active Pt surface sites. We postulate that this selective LSPR-induced energizing of the Pt active centres ultimately leads to the selective heating of the most-abundant reaction intermediate (CO) on the catalyst surface, which results in elevated reactions rates[39]. This heating of adsorbed CO can take place either through direct phonon–phonon interactions with the hot Pt atoms or a LSPR-field-mediated vibronic coupling induced by direct vertical electronic excitations in the Pt–CO surface complexes[18,24].

In conclusion, we have demonstrated the ability to control the energy flow in plasmonic systems at the nanoscale level through the targeted synthesis of multicomponent plasmonic nanostructures. By completely coating a plasmonic metal (Ag) nanocube that possesses a low imaginary dielectric function with a few atomic layers of a catalytic metal (Pt) that possesses a high imaginary dielectric function, a channel for plasmon decay was introduced and led to the dissipation of light energy through the thin Pt shell. This energy was then used to drive a photochemical reaction on the Pt centres. This well-defined model system allowed us to demonstrate plasmon-driven energy transfer and catalysis on non-plasmonic surfaces. We believe that the underlying physical concepts discussed in this work will motivate the rational design of other multicomponent plasmonic systems to control energy flow in plasmonic, energy harvesting and photocatalytic applications.

Methods

Methods and any associated references are available in the online version of the paper.

Received 16 March 2017; accepted 6 June 2017;
published online 17 July 2017

References

1. Christopher, P., Xin, H. & Linic, S. Visible-light-enhanced catalytic oxidation reactions on plasmonic silver nanostructures. *Nat. Chem.* **3,** 467–472 (2011).
2. Mukherjee, S. *et al.* Hot electrons do the impossible: plasmon-induced dissociation of H_2 on Au. *Nano Lett.* **13,** 240–247 (2013).
3. Xiao, Q. *et al.* Alloying gold with copper makes for a highly selective visible-light photocatalyst for the reduction of nitroaromatics to anilines. *ACS Catal.* **6,** 1744–1753 (2016).
4. Kale, M. J., Avanesian, T. & Christopher, P. Direct photocatalysis by plasmonic nanostructures. *ACS Catal.* **4,** 116–128 (2014).
5. Kim, Y., Dumett Torres, D. & Jain, P. K. Activation energies of plasmonic catalysts. *Nano Lett.* **16,** 3399–3407 (2016).
6. Christopher, P., Xin, H., Marimuthu, A. & Linic, S. Singular characteristics and unique chemical bond activation mechanisms of photocatalytic reactions on plasmonic nanostructures. *Nat. Mater.* **11,** 1044–1050 (2012).
7. Huang, Y.-F. *et al.* Activation of oxygen on gold and silver nanoparticles assisted by surface plasmon resonances. *Angew. Chem. Int. Ed.* **53,** 2353–2357 (2014).
8. Marimuthu, A., Zhang, J. & Linic, S. Tuning selectivity in propylene epoxidation by plasmon mediated photo-switching of Cu oxidation state. *Science* **339,** 1590–1593 (2013).
9. Kelly, K. L., Coronado, E., Zhao, L. L. & Schatz, G. C. The optical properties of metal nanoparticles: the influence of size, shape, and dielectric environment. *J. Phys. Chem. B* **107,** 668–677 (2002).
10. Link, S. & El-Sayed, M. A. Spectral properties and relaxation dynamics of surface plasmon electronic oscillations in gold and silver nanodots and nanorods. *J. Phys. Chem. B* **103,** 8410–8426 (1999).
11. Linic, S., Christopher, P. & Ingram, D. B. Plasmonic-metal nanostructures for efficient conversion of solar to chemical energy. *Nat. Mater.* **10,** 911–921 (2011).

12. Linic, S., Aslam, U., Boerigter, C. & Morabito, M. Photochemical transformations on plasmonic metal nanoparticles. *Nat. Mater.* **14,** 567–576 (2015).
13. Manjavacas, A., Liu, J. G., Kulkarni, V. & Nordlander, P. Plasmon-induced hot carriers in metallic nanoparticles. *ACS Nano* **8,** 7630–7638 (2014).
14. Sundararaman, R., Narang, P., Jermyn, A. S., Goddard, W. A. III & Atwater, H. A. Theoretical predictions for hot-carrier generation from surface plasmon decay. *Nat. Commun.* **5,** 5788 (2014).
15. Hammer, B. & Nørskov, J. K. Why gold is the noblest of all the metals. *Nature* **376,** 238–240 (1995).
16. Hammer, B. & Nørskov, J. K. in *Advances in Catalysis* Vol. 45 (eds Bruce, C. & Gates, H. K.) 71–129 (Academic, 2000).
17. Boerigter, C., Campana, R., Morabito, M. & Linic, S. Evidence and implications of direct charge excitation as the dominant mechanism in plasmon-mediated photocatalysis. *Nat. Commun.* **7,** 10545 (2016).
18. Boerigter, C., Aslam, U. & Linic, S. Mechanism of charge transfer from plasmonic nanostructures to chemically attached materials. *ACS Nano* **10,** 6108–6115 (2016).
19. Brown, A. M., Sundararaman, R., Narang, P., Goddard, W. A. & Atwater, H. A. Nonradiative plasmon decay and hot carrier dynamics: effects of phonons, surfaces, and geometry. *ACS Nano* **10,** 957–966 (2016).
20. Bernardi, M., Mustafa, J., Neaton, J. B. & Louie, S. G. Theory and computation of hot carriers generated by surface plasmon polaritons in noble metals. *Nat. Commun.* **6,** 7044 (2015).
21. Griffin, S. *et al.* Imaging energy transfer in Pt-decorated Au nanoprisms via electron energy-loss spectroscopy. *J. Phys. Chem. Lett.* **7,** 3825–3832 (2016).
22. Amendola, V., Saija, R., Maragò, O. M. & Antonia Iatì, M. Superior plasmon absorption in iron-doped gold nanoparticles. *Nanoscale* **7,** 8782–8792 (2015).
23. Alayoglu, S., Nilekar, A. U., Mavrikakis, M. & Eichhorn, B. Ru–Pt core–shell nanoparticles for preferential oxidation of carbon monoxide in hydrogen. *Nat. Mater.* **7,** 333–338 (2008).
24. Kale, M. J., Avanesian, T., Xin, H., Yan, J. & Christopher, P. Controlling catalytic selectivity on metal nanoparticles by direct photoexcitation of adsorbate–metal bonds. *Nano Lett.* **14,** 5405–5412 (2014).
25. Zheng, Z., Tachikawa, T. & Majima, T. Single-particle study of Pt-modified Au nanorods for plasmon-enhanced hydrogen generation in visible to near-infrared region. *J. Am. Chem. Soc.* **136,** 6870–6873 (2014).
26. Zheng, Z., Tachikawa, T. & Majima, T. Plasmon-enhanced formic acid dehydrogenation using anisotropic Pd–Au nanorods studied at the single-particle level. *J. Am. Chem. Soc.* **137,** 948–957 (2014).
27. Swearer, D. F. *et al.* Heterometallic antenna–reactor complexes for photocatalysis. *Proc. Natl Acad. Sci. USA* **113,** 8916–8920 (2016).
28. Zhang, C. *et al.* Al–Pd nanodisk heterodimers as antenna–reactor photocatalysts. *Nano Lett.* **16,** 6677–6682 (2016).
29. Xiao, Q. *et al.* Visible light-driven cross-coupling reactions at lower temperatures using a photocatalyst of palladium and gold alloy nanoparticles. *ACS Catal.* **4,** 1725–1734 (2014).
30. Li, Z. *et al.* Reversible modulation of surface plasmons in gold nanoparticles enabled by surface redox chemistry. *Angew. Chem.* **54,** 8948–8951 (2015).
31. Aslam, U. & Linic, S. Kinetic trapping of immiscible metal atoms into bimetallic nanoparticles through plasmonic visible light-mediated reduction of a bimetallic oxide precursor: case study of Ag–Pt nanoparticle synthesis. *Chem. Mater.* **28,** 8289–8295 (2016).
32. Evanoff, D. D. & Chumanov, G. Size-controlled synthesis of nanoparticles. 2. Measurement of extinction, scattering, and absorption cross sections. *J. Phys. Chem. B* **108,** 13957–13962 (2004).
33. Langhammer, C., Kasemo, B. & Zorić, I. Absorption and scattering of light by Pt, Pd, Ag, and Au nanodisks: absolute cross sections and branching ratios. *J. Chem. Phys.* **126,** 194702 (2007).
34. Kahlich, M. J., Gasteiger, H. A. & Behm, R. J. Kinetics of the selective CO oxidation in H_2-rich gas on Pt/Al_2O_3. *J. Catal.* **171,** 93–105 (1997).
35. Manasilp, A. & Gulari, E. Selective CO oxidation over Pt/alumina catalysts for fuel cell applications. *Appl. Catal. B* **37,** 17–25 (2002).
36. Boccuzzi, F. *et al.* Gold, silver and copper catalysts supported on TiO_2 for pure hydrogen production. *Catal. Today* **75,** 169–175 (2002).
37. Khurgin, J. B. How to deal with the loss in plasmonics and metamaterials. *Nat. Nanotech.* **10,** 2–6 (2015).
38. Kreibig, U. & Vollmer, M. *Optical Properties of Metal Clusters* (Springer Science & Business Media, 2013).
39. Nilekar, A. U., Alayoglu, S., Eichhorn, B. & Mavrikakis, M. Preferential CO oxidation in hydrogen: reactivity of core–shell nanoparticles. *J. Am. Chem. Soc.* **132,** 7418–7428 (2010).

Acknowledgements

This work was primarily supported by the National Science Foundation (NSF) (CBET-1437601 and CBET- 1702471). The synthesis was developed with the support of the US Department of Energy, Office of Basic Energy Science, Division of Chemical Sciences (FG-02-05ER15686). Secondary support for the development of analytical tools used to analyse the data was provided by NSF (CBET-1436056 and CHE- 1362120). The electron microscopy measurements were supported by the University of Michigan College of Engineering and by NSF (DMR-0723032). S.L. also acknowledges the partial support of the Technical University Munich – Institute for Advance Study.

Author contributions

U.A. and S.L. developed the project. U.A. carried out the syntheses, characterization, optical measurements and reactor studies. S.C. performed all the optical simulations. All the authors wrote the manuscript and Supplementary Information.

Additional information

Supplementary information is available in the online version of the paper. Reprints and permissions information is available online at www.nature.com/reprints. Publisher's note: Springer Nature remains neutral with regard to jurisdictional claims in published maps and institutional affiliations. Correspondence and requests for materials should be addressed to S.L.

Competing financial interests

The authors declare no competing financial interests.

Methods

Nanoparticle synthesis. To synthesize Ag nanocubes, 10 ml of ethylene glycol (semigrade (VWR International)) were heated to 140 °C for 1 h. A 36 mM aqueous HCl solution (80 µl) was added to the reaction vessel followed by 5 ml of a 10 mg ml^{-1} solution of polyvinylpyrrolidone (PVP, M_W = 55,000 (Sigma-Aldrich)) and 2 ml of a 25 mg ml^{-1} solution of $AgNO_3$ (ultrapure grade 99.5% (Acros Organics)) in ethylene glycol. A ventilated cap was placed on the reaction vessel and the mixture was allowed to heat for ~24 h. After this, the ventilated cap was exchanged for a sealed cap to prevent O_2 from entering the system. The reaction then took place over ~8 h to form Ag nanocubes. The nanocubes were purified via centrifugation at 8,000 revolutions per minute (r.p.m.) with a 1:10 water-to-acetone mixture twice and re-dispersed in deionized (DI) water.

Ag–Pt nanocubes were synthesized by diluting one-tenth of a solution of Ag nanocubes with 3 ml of DI water that contained 50 mg of PVP under continuous mixing. A reducing solution, 100 mg of ascorbic acid (reagent grade (Sigma-Aldrich)) mixed with 3 ml of DI water and 600 µl of an aqueous 1.25 M NaOH solution, was then added to the reaction vessel. A solution of the Pt precursor, 12 mg of K_2PtCl_4 (99.99% (Sigma-Aldrich)) in 16 ml of DI water, was slowly injected via a syringe pump at a rate of 4 ml h^{-1} for 4 h. Every 2 h, 50 µl of an aqueous 1.25 M NaOH solution was added to the reaction vessel. The nanoparticles were purified via centrifugation at 10,000 r.p.m. with DI water twice.

Nanoparticle characterization. All STEM and EDS were performed using a JEOL 3100 double Cs-corrected TEM/STEM operated at an accelerating voltage of 300 kV. Samples were prepared by drop casting a dilute solution of nanoparticles/catalyst onto a 200 mesh carbon-on-copper grid. Elemental line profiles and maps were generated using the Ag Lα and Pt M transition peaks in EDS.

DRIFTS was performed using a Nicolet iS 50 spectrometer equipped with a HgCdTe detector, a Harrick Praying Mantis diffuse reflectance cell and a Harrick high-temperature reaction chamber with a dome cap and KBr windows. The bench and diffuse-reflectance cell were purged continuously with N_2 gas and data were acquired by averaging 128 scans at a resolution of 4 cm^{-1}. Additional details regarding specific experiments are provided in Supplementary Section 1.

Optical extinction measurements were taken using an Evolution 300 spectrophotometer. All the samples were prepared to provide a maximum extinction fraction of 0.5 in 3 ml cuvettes. Optical absorption measurements were performed using an optical integrating sphere from LabSphere. Liquid samples in 3 ml cuvettes were placed in the middle of the integrating sphere and monochromatic light from 300 to 900 nm was shone through the sample and collected using a photodiode detector (Newport Corporations) at the bottom of the sphere. Monochromated light was generated by a 1,000 W Xe lamp and a Conerstone 260 monochromator.

Optical simulations. Optical simulations were preformed using the Wave Optics module on COMSOL Multiphysics finite-element-based software. The model systems included a three-dimensional (3D) nanoparticle surrounded by air and a perfectly matched layer to absorb the scattered field from a plane-wave incident on the 3D nanoparticle. The width of the region of air that surrounds the nanoparticles was set to half the wavelength of the incident plane wave and optical data for Ag and Pt were taken from the COMSOL Optical Materials database. More details for specific calculations are provided in Supplementary Sections 3 and 4.

Reactor studies. Catalyst were prepared by depositing a colloidal dispersion of nanoparticles onto an α-Al_2O_3 (Alfa Aesar) support. Reactor studies were performed in a Harrick high-temperature reactor with a 1 cm^2 SiO_2 window for visible-light irradiation of the catalyst. Catalysts were pre-treated with 100 sccm of air at 250 °C for 3 h, cooled to 200 °C under a 100 sccm N_2 flow and then exposed to 100 sccm of the reactant mixture (3% CO, 2% O_2, 75% H_2 and balance N_2). The system was allowed to reach a steady state overnight (~12 h) and data were collected for a range of different temperatures under both thermal and photothermal conditions. The light source used for the catalyst illumination was a Dolan-Jenner Fiber-Lite 180 with a 150 W, 21 V halogen (EKE) lamp. Gas-flow rates were controlled using Cole-Parmer mass flow controllers. Product gases were analysed using a Varian CP 3800 gas chromatograph with temperature conductivity detectors, an Agilent 7890B/5977A gas chromatograph with a mass selective detector and a Hiden HPR-20 mass spectrometer. Wavelength-dependent experiments were performed using shortpass and longpass filters from Edmund Optics. The intensity of the light source was measured using a Newport thermopile detector.

Data availability. The data that support the plots within this paper and other findings of this study are available from the corresponding author on reasonable request.